Acoustic Non-Abelian Topological Insulator Induced by Artificial SU(2) Gauge Fields

Haonan Wang[1,†], Hui Liu[1,†,*], Zhancheng Li[1], Yuanshuo Liu[1], Weiyin Deng[2], Hua Cheng[1,*], Zhengyou Liu[2], and Shuqi Chen[1,3,4*]

[1]The Key Laboratory of Weak Light Nonlinear Photonics, Ministry of Education, School of Physics and TEDA Institute of Applied Physics, Nankai University, Tianjin 300071, China

[2]Key Laboratory of Artificial Micro- and Nanostructures of Ministry of Education and School of Physics and Technology, Wuhan University, Wuhan 430072, China

[3]School of Materials Science and Engineering, Nankai University, Tianjin 300350, China

[4]The Collaborative Innovation Center of Extreme Optics, Shanxi University, Taiyuan 030006, China

†These authors contributed equally to this work.

*Corresponding author: hliu@nankai.edu.cn, hcheng@nankai.edu.cn and schen@nankai.edu.cn

Non-Abelian topological insulator, arising from non-Abelian gauge field, not only links to particle physics and the strong and weak forces of nature, but also creates coveted topological phenomena with remarkable properties. Although significant efforts have been made for developing artificial non-Abelian gauge fields, few of them applied to momentum space to realize non-Abelian topological insulators. Here, we propose a scheme to create artificial SU(2) gauge fields in phononic crystals. By implement this scheme to a non-Abelian Hofstadter model, we overcome the challenge of constructing an analog of non-Abelian magnetic field in momentum space that open nontrivial band gaps. We experimentally realize and observe such non-Abelian topological insulating phase in a phononic crystal. Furthermore, we experimentally investigate the spin rotation and flipping

phenomena of non-Abelian topological boundary states along a specific plane of the Bloch sphere, which are linked to the signatures of the underlying non-Abelian gauge field. Our work not only opens the door to the realization and characterization of non-Abelian topological insulator, but also provides a reconfigurable platform for exploring non-Abelian physics in classical system.

Artificial gauge fields create topological physics with extraordinary topological states that forms the backbone of many anti-interference information transmission and device designs [1,2]. Such artificial gauge fields, known as Berry curvature in topological physics, can be understood through the Abelian (commutative) or non-Abelian (non-commutative) properties of the correlation groups. Since the discovery of topological physics in condensed matter systems, most topological systems have been built on mimicking the interaction between electrons and U(1) gauge fields, following the Abelian properties of electromagnetism. So far, great success has been achieved in creating novel topological phases of matter in broader systems without intrinsic electronic properties, such as cold atoms [3,4], photonic systems [5,6] and acoustic systems [7–13], by constructing artificial Abelian gauge fields in lattice structures. Some novel topological phases, such as the quadrupole topological insulator protected by momentum-space nonsymmorphic symmetries, have been successfully realized using artificial Abelian gauge fields [14]. The fanatical pursuit of such topological phases and phenomena is due to the fact that besides their clear links to electromagnetism, there are more practical motivations: the robustness properties of topological systems are expected to revolutionize traditional devices.

In contrast, non-Abelian topology remains relatively underexplored, though it is attracting growing attention due to its potential to significantly expand the theoretical frameworks and phenomena of topological physics [15–21]. In nature, non-Abelian gauge fields, mediating more complex strong and weak interactions, require more internal states and non-commutative matrix-valued gauge potentials. They have been

artificially constructed in various experimental platforms such as cold atoms [22], optics [23–25] and circuits [26–28], with the rapid progress in the design and implementation of artificial gauge fields. A series of extraordinary physical phenomena induced by artificial non-Abelian gauge fields, such as non-Abelian holonomies [29,30], non-Abelian Aharonov-Bohm effect [26,31], non-Abelian topological order [32] and Yang monopoles [33,34], have been found experimentally. However, these previously realized non-Abelian gauge fields are not analogs of magnetic fields in momentum space, namely Berry curvature, which lies at the heart of topological physics. Thus, they cannot open non-trivial band gaps and realize a non-Abelian topological insulator. Recently, theoretical schemes have been proposed to realize non-Abelian topological insulators by engineering non-Abelian artificial gauge fields in lattice systems to construct non-Abelian magnetic Brillouin zones [35–38]. However, the experimental realization of non-Abelian topological insulators and their topological phenomena remain elusive due to the need for complex matrix couplings and non-Abelian magnetic Brillouin zones.

In this letter, we develop a scheme to create artificial SU(2) gauge fields in phononic crystals, where layer degrees of freedom are employed to implement complex matrix-valued couplings. We realize a non-Abelian topological insulator in a phononic crystal by implementing this scheme in a non-Abelian Hofstadter model, which constructs a non-Abelian magnetic Brillouin zone and open nontrivial topological gaps. We experimentally observed a pair of boundary states with opposite spins in the narrow topological gap, induced by an artificial SU(2) gauge field in momentum space. We further characterized their properties, including spin rotation and flipping along a specific plane of the Bloch sphere, which bear the unique signature of the non-Abelian gauge field.

Tight-binding model for acoustic non-Abelian topological insulator

Two key elements are required for us to realize a non-Abelian topological insulator: artificial SU(2) lattice gauge fields and analogs of non-Abelian magnetic fields that

induce non-trivial energy gaps. Starting with the tight-binding model, we present a scheme to equivalently create complex matrix couplings corresponding to the elements of the SU(2) matrix group, as shown in Fig. 1(a). We introduce layer degrees of freedom as the pseudospin denoted by $\uparrow,\downarrow$. The other two pseudospin copies (lowercase and uppercase letters) are used to construct equivalent conjugate imaginary couplings. In the basis $(a_\uparrow, a_\downarrow, A_\uparrow, A_\downarrow, b_\uparrow, b_\downarrow, B_\uparrow, B_\downarrow)^{\mathrm{T}}$, the link variables U_μ ($\mu = x, y, z$), consist of purely real couplings, intralayer couplings t_0 and interlayer couplings $t_{1,2,3}$ (positive in red, negative in blue), as shown in the upper panel of Fig. 1(a). By applying a unitary transformation $S = \frac{1}{\sqrt{2}}\begin{pmatrix} \mathrm{I}_2 \otimes [1, \mathrm{i}] \otimes \mathrm{I}_2 \\ \mathrm{I}_2 \otimes [1, -\mathrm{i}] \otimes \mathrm{I}_2 \end{pmatrix}$, the basis is converted to a new one $(|+\mathrm{i}\rangle, |-\mathrm{i}\rangle)^{\mathrm{T}}$, which spans two decoupled conjugate subspaces, $|+\mathrm{i}\rangle = (a_\uparrow + \mathrm{i}A_\uparrow, a_\downarrow + \mathrm{i}A_\downarrow, b_\uparrow + \mathrm{i}B_\uparrow, b_\downarrow + \mathrm{i}B_\downarrow)/\sqrt{2}$ and $|-\mathrm{i}\rangle = |+\mathrm{i}\rangle^*$, as shown in the lower panel of Fig. 1(a). Each subspace provides link variables V_μ between adjacent lattice sites, where $V_x(\omega) = \mathrm{e}^{-\mathrm{i}\omega\sigma_x}, V_y(\theta) = \mathrm{e}^{-\mathrm{i}\theta\sigma_y}, V_z(\phi) = \mathrm{e}^{-\mathrm{i}\phi\sigma_z}$ are the elements of SU(2) matrix group. $\omega = \arctan(t_1/t_0)$, $\theta = \arctan(t_2/t_0)$ and $\phi = \arctan(t_3/t_0)$ correspond to half of the rotation angle of the Bloch sphere along the σ_x, σ_y, σ_z axes, respectively. By tuning the ratios $t_{1,2,3}/t_0$, arbitrary artificial SU(2) gauge fields can be achieved.

We select two types of the matrix couplings U_y and U_z to construct non-Abelian magnetic field analogs in non-Abelian Hofstadter models. The tight-binding model in Fig. 1(b) yields the Hamiltonian:

$$H(\theta,\phi) = -\sum_{m,n} t_x a^\dagger_{m+1,n} U_y(n\theta) a_{m,n} + t_y a^\dagger_{m,n+1} U_z(-m\phi) a_{m,n} + \mathrm{H.c.}, \qquad (1)$$

where $a_{m,n} = \left[a_{m,n,\uparrow}, a_{m,n,\downarrow}, A_{m,n,\uparrow}, A_{m,n,\downarrow}\right]^{\mathrm{T}}$ is the annihilation operator at the (m,n) site. t_x (t_y) represents the hopping amplitude along the x (y) direction, which is set to

$t_x = t_y = -1$ unless otherwise noted. Through a similar unitary transformation, we derive the non-Abelian Hofstadter model with link variables V_y and V_z in $|+\mathrm{i}\rangle$ subspace, as shown in Fig. 1(c). This model describes two-dimensional spin-1/2 particles on a square lattice under an artificial SU(2) 'magnetic field'. Hamiltonian details are provided in Supplemental Material Sec. I [42].

To investigate the properties of this non-Abelian Hofstadter model, we only need to consider the Hamiltonian in $|+\mathrm{i}\rangle$ subspace, which reads:

$$h(\theta,\phi) = -\sum_{m,n} t_x a^{\dagger}_{m+1,n} V_y(n\theta) a_{m,n} + t_y a^{\dagger}_{m,n+1} V_z(-m\phi) a_{m,n} + \mathrm{H.c.}, \tag{2}$$

$V_y(n\theta) = \mathrm{e}^{-\mathrm{i}n\theta\sigma_y}$ and $V_z(-m\phi) = \mathrm{e}^{\mathrm{i}m\phi\sigma_z}$ represent gradient-varying link variables applied in x and y directions, respectively. The link variable $V_z(-m\phi)$, acting as the intrinsic spin-orbit coupling, provides opposite fluxes $\pm\phi$ for each spin sector. Whereas, $V_y(n\theta)$ resembles Rashba-type spin-orbit coupling, which mixes the spin components. Two types of link variables conspire to yield the artificial SU(2) gauge field, with gauge potential given as $\boldsymbol{A} = (-n\theta\sigma_y, m\phi\sigma_z, 0)$. Here, $\theta = 2\pi\, p_\theta / q_\theta$ and $\phi = 2\pi\, p_\phi / q_\phi$ are effective flux penetrating the unit cell normal to x and y directions, respectively, with integers $p_\theta, q_\theta, p_\phi, q_\phi$. The model in Fig. 1(c) adopts a $q_\phi \times q_\theta$ magnetic unit cell and its magnetic Brillouin zone is defined as $k_x \in [0, 2\pi/q_\phi)$, $k_y \in [0, 2\pi/q_\theta)$. Two non-commuting link variables jointly drive the artificial gauge field into the non-Abelian regime for most parameters (θ,ϕ). However, it reduces to the Abelian regime at certain specific parameter values, i.e. $\theta \in \{0, \pi\}$, $\phi \in \{0, \pi\}$, or $\{\theta, \phi\} \in \{\pi/2, 3\pi/2\}$. The relevant magnetic-field effects and their nature can be detected by the Wilson loop (see End Matter for details).

Acoustic implementation for a non-Abelian topological insulator

We now consider a phononic crystal implementation of a non-Abelian topological insulator induced by the artificial SU(2) gauge fields. We employ two link variables, $U_y(\pi/2)$ and $U_z(-4\pi/3)$, as examples to present the key components for constructing acoustic SU(2) gauge fields, as illustrated in Figs. 2(a) and 2(b). Each site consists of four layers of cuboid acoustic cavities (height $h_0 = 45$ mm, width $w = 10$ mm), serving as artificial atoms with an onsite frequency $f_0 = 3830$ Hz. By adjusting the position and diameter of the intralayer and interlayer tubes, the sign (positive in red, negative in blue) and strength of the couplings can be precisely controlled, respectively. For $U_y(\pi/2)$, only interlayer tubes with diameter $d_1 = 3.6$ mm exist, corresponding to a coupling strength of 106 Hz and $\theta = \pi/2$. For $U_z(-4\pi/3)$, intralayer ($d_2 = 1.9$ mm) and interlayer ($d_3 = 3.2$ mm) tubes yield the coupling strength of -53 Hz and 92 Hz, respectively, with their ratio yielding $\phi = -4\pi/3$. These acoustic link variables agree well with the tight-binding model (Supplemental Material Sec. II [42]). By fine-tuning the coupling ratio, arbitrary artificial SU(2) gauge fields can be achieved. Based on the tight-binding model, we develop the acoustic Hofstadter model, where the link variables $U_y(\theta)$ and $U_z(\phi)$ vary with gradients along the x and y directions, respectively. We take $(\theta,\phi) = (\pi, 2\pi/3)$ and $(\theta,\phi) = (\pi/2, 2\pi/3)$ for the Abelian and non-Abelian cases, as shown in Figs. 2(c) and 2(d). Their unit cell size is $ma \times na$, where m (n) is the site along the x (y) direction and $a = 32$ mm is the distance between adjacent sites. The two cases differ in the flux $\theta = \pi$ adopted in the Abelian case, where all x-direction link variables, $U_y(2\pi)$ and $U_y(\pi)$, reduce to the identity matrix and commute with y-direction link variables. Consequently, the Wilson loop (accumulated phase along a closed path) around each plaquette becomes Abelian, driving the system into the Abelian regime. In non-Abelian cases, x- and y-direction link variables remain non-commuting, keeping Wilson loop non-Abelian. The Hamiltonians and structural

details are provided in Supplemental Material Secs. III and IV [42], respectively.

Each subspace hosts a total of $m\times n\times 2$ bulk bands, which are $m\times n$ Kramers partners. Since the system exhibits chiral symmetry for even $q_\theta q_\phi$, the simulated bulk bands of the Abelian and non-Abelian cases symmetric around 'zero energy', resulting in the double Dirac points (purple spheres) at 'zero energy' frequency, as shown in Figs. 2(e) and 2(f), respectively. Under an Abelian gauge field, multiple topologically nontrivial band gaps emerge, corresponding to the quantum spin Hall effect (QSHE). For the non-Abelian case, the SU(2) gauge field opens multiple more complex and narrower band gaps, indicating a non-Abelian topological insulator with richer topological properties beyond the QSHE. Such artificial non-Abelian gauge fields in momentum space, known as the non-Abelian Berry curvature, induces nontrivial non-Abelian topology, which is expressed as:

$$\boldsymbol{F}_{xy}^{\pm}=\partial_x A_y^{\pm}-\partial_y A_x^{\pm}-\mathrm{i}\left[A_x^{\pm},A_y^{\pm}\right]. \tag{3}$$

Here, $\boldsymbol{A}_{mn}^{\pm}=\mathrm{i}\left\langle\pm\phi_m(k)\right|\nabla_k\left|\pm\phi_n(k)\right\rangle$ is the non-Abelian Berry connection and $\left|\pm\phi_i\right\rangle$ represent the Bloch states below the i-th gap of the $q_\phi\times q_\theta$ unit cell. For the non-Abelian case $\left[A_x^{\pm},A_y^{\pm}\right]\neq 0$, the non-Abelian Berry curvature, which takes the same form as the Yang-Mills gauge field strength [39], can be interpreted as an analog of the non-Abelian magnetic field. The topological invariants, labeled in right of the bulk bands, are captured by integrating the non-Abelian Berry curvature (Supplemental Material Sec. V [42]). Beyond the band structure, the non-Abelian Hofstadter butterfly spectrum reveals a more complex fractal structure with narrow topological gaps, distinct from the Abelian counterpart (see End Matter).

Non-Abelian boundary states with spin-rotation characteristics

To demonstrate the topological properties of the boundary states induced by artificial non-Abelian gauge fields, we 3D-printed acoustic Abelian and non-Abelian topological insulator samples. Boundary states are excited by four per-layer acoustic sources at the hard boundary, with amplitude and phase controlled independently via power amplifiers

and phase shifters. Sound pressure fields are measured by sequentially placing a subwavelength microphone into each boundary cavity, with sound signals recorded using an oscilloscope. Samples and experimental details are given in the End Matter. Figure 3 presents the measured boundary states within the lowest energy gap along the *y*-boundary. For the Abelian topological insulator, the measured projected band dispersions (colormaps) agree well with simulations, as shown in Fig. 3(a). The simulated helical boundary states and bulk states are denoted by dashed lines and gray regions, respectively. By projecting the boundary states extracted from experiments and simulations onto the Bloch sphere, we find that the spin of the boundary state lies along the σ_z direction of the Bloch sphere, as shown in Fig. 3(b). The Abelian topological boundary states exhibit the QSHE, in which pure spin-up and spin-down states experience opposite magnetic fluxes and propagate helically along the boundaries in opposite directions. In contrast, the non-Abelian case involves spin interactions related to the non-Abelian gauge field, yielding narrower gaps and distinct boundary state properties. The measured and simulated projected band dispersions are presented in Fig. 3(c). The boundary states with given k values are projected onto the Bloch sphere, as shown in Fig. 3(d). The spin projections of non-Abelian boundary states lie on a specific plane $\sigma_y - \sigma_z$ within the Bloch sphere rather than along a certain axis as in the Abelian case. Furthermore, as k_y varies, the spin polarizations of non-Abelian helical boundary states exhibit a spin-rotation behavior near the plane $\sigma_y - \sigma_z$. Owing to time-reversal symmetry, the helical boundary states at opposite *k* are mutually orthogonal, marked in red and blue. The spin-rotation characteristics of the non-Abelian boundary states also remain robust against perturbations (Supplemental Material Sec. VIII [42]). The spin-rotation behavior along a specific plane arises from the chosen non-Abelian gauge potential $\boldsymbol{A} = (-n\theta\sigma_y, m\phi\sigma_z, 0)$. In the symmetric gauge, adopting other Pauli matrix combinations in $\boldsymbol{A}$ shift the spin-rotation plane, while other topological features remain unchanged (Supplemental Material Sec. IX [42]). The spin-rotation angle can

be adjusted by modifying the boundaries (Supplemental Material Sec. X [42]). Thus, beyond inheriting the helical transmission of Abelian boundary states, the non-Abelian boundary states further manifest non-Abelian gauge field effects through spin interactions. The measured Abelian and non-Abelian boundary states along the x direction are given in the Supplemental Material Sec. XI [42].

Spin flipping in non-Abelian boundary states

To further verify the spin interaction under artificial non-Abelian gauge fields, we experimentally investigate the spin flipping of non-Abelian boundary states through an H-shaped phononic crystal with four channels. Figure 4(a) schematizes the H-shaped structure, consisting of two non-Abelian topological insulator blocks connected by a narrow bridge (Supplemental Material Sec. XII [42]). Channels 1-4 support y-direction boundary states shown in Fig. 3(c). In a uniform periodic structure, the spin polarization of non-Abelian boundary states is position-independent and does not flip along a single channel. However, when the structure is bent into an H-shaped structure, the spin interactions between the boundary waves propagating along the upper and lower sides of the narrow bridge become activated, inducing boundary state spin flipping. Exciting a boundary state projected onto the upper half of the Bloch sphere in channel 1 (green star) allows transmission only to channels 2 and 3 (red arrows), while transmission to channel 4 requires the state flipping to its orthogonal spin-projected counterpart (blue arrow). Figure 4(b) presents the simulated transmission at 3564 Hz. Spin flipping oscillates periodically with the narrow-bridge length L_m, which modulates the interference phase difference between transmitted and reflected waves propagating along the bridge [40,41]. For $L_m = 2a$, the simulated and experimental top-layer sound field distributions are plotted in Figs. 4(c) and 4(d), respectively, confirming wave transmission from channel 1 to channel 4. Sound pressure responses of each layer at the four channels are measured and projected into spin space, directly revealing spin-flipping behavior in Figs. 4(e) and 4(f). Sound waves with upper Bloch-sphere spin projection preserve their spin in channels 2 and 3, yet flip to an orthogonal state in

channel 4. This spin-flipping process occurs on the plane $\sigma_y - \sigma_z$ (blue plane), arising from the spin interactions induced by the non-Abelian gauge fields. Tuning the spin interactions within the H-shaped waveguide enables spin manipulation and acoustic beam splitting (Supplemental Material XIII [42]).

Conclusion

We have developed a scheme to construct artificial SU(2) gauge fields in spinless system, which can realize a non-Abelian topological insulator in a phononic crystal. In addition, we have experimentally observed the features of boundary states in the non-Abelian topological insulator, including spin rotation and flipping along a specific plane of the Bloch sphere, which exhibit the signatures of the underlying non-Abelian gauge field. This work implies two fundamental aspects that differ from earlier works on artificial non-Abelian gauge fields. Firstly, we propose a novel scheme for constructing artificial SU(2) gauge fields in spinless systems by utilizing layer degrees of freedom. Secondly, we realize and characterize a non-Abelian topological insulator induced by artificial SU(2) gauge fields for the first time. This scheme provides a reliable approach for exploring non-Abelian physics in classical systems. Our results are expected to stimulate broad interest in expanding the theoretical frameworks and exploring the phenomena of topological physics.

Data availability

All relevant data of this study are available from the corresponding author upon reasonable request.

Acknowledgments

This work was supported by the National Key Research and Development Program of China (Nos. 2022YFA1404501 and 2022YFA1404900), the National Natural Science Foundation of China (Nos. 12304486, 12192253, 12474331, W2441005, and 12534014), and the Natural Science Foundation of Tianjin (Nos. 23JCQNJC01450).

Author contributions

H.C., H.L., and S.C. conceived the idea. H.W., H.L., Y.L., and H.C. performed the theoretical analysis and numerical simulations and experiments. H.W., H.L., Z.L., Y.L., W.D., H.C., Z.L., and S.C. prepared the manuscript. All the authors contributed to the analyses and discussions of the manuscript.

Competing interests

The authors declare no competing financial interests.

References

[1] H. Xue, Y. Yang, and B. Zhang, Topological acoustics, Nat. Rev. Mater. **7**, 974 (2022).

[2] X. Zhang, F. Zangeneh-Nejad, Z. Chen, M. Lu, and J. Christensen, A second wave of topological phenomena in photonics and acoustics, Nature **618**, 687 (2023).

[3] N. Goldman, G. Juzeliūnas, P. Öhberg, and I. B. Spielman, Light-induced gauge fields for ultracold atoms, Reports Prog. Phys. **77**, 126401 (2014).

[4] J. C. Halimeh, M. Aidelsburger, F. Grusdt, P. Hauke, and B. Yang, Cold-atom quantum simulators of gauge theories, Nat. Phys. **21**, 25 (2025).

[5] R. Barczyk, L. Kuipers, and E. Verhagen, Observation of Landau levels and chiral edge states in photonic crystals through pseudomagnetic fields induced by synthetic strain, Nat. Photonics **18**, 574 (2024).

[6] H. Cheng et al., Vortical Reflection and Spiraling Fermi Arcs with Weyl Metamaterials Supplementary Information for Vortical, Phys. Rev. Lett. **125**, 93904 (2020).

[7] M. Xiao, W.-J. Chen, W.-Y. He, and C. T. Chan, Synthetic gauge flux and Weyl points in acoustic systems, Nat. Phys. **11**, 920 (2015).

[8] X. Wen, C. Qiu, Y. Qi, L. Ye, M. Ke, F. Zhang, and Z. Liu, Acoustic Landau

quantization and quantum-Hall-like edge states, Nat. Phys. **15**, 352 (2019).

[9] B. Xie, H. Liu, H. Cheng, Z. Liu, S. Chen, and J. Tian, Experimental Realization of Type-II Weyl Points and Fermi Arcs in Phononic Crystal, Phys. Rev. Lett. **122**, 104302 (2019).

[10] L. Ye, Q. Wang, Z. Fu, H. He, X. Huang, M. Ke, J. Lu, W. Deng, and Z. Liu, Hinge Modes of Surface Arcs in a Synthetic Weyl Phononic Crystal, Phys. Rev. Lett. **133**, 126602 (2024).

[11] J. Wu, R. Zheng, J. Liang, M. Ke, J. Lu, W. Deng, X. Huang, and Z. Liu, Spin-Dependent Localization of Helical Edge States in a Non-Hermitian Phononic Crystal, Phys. Rev. Lett. **133**, 126601 (2024).

[12] Z. Cheng, Y.-J. Guan, H. Xue, Y. Ge, D. Jia, Y. Long, S.-Q. Yuan, H.-X. Sun, Y. Chong, and B. Zhang, Three-dimensional flat Landau levels in an inhomogeneous acoustic crystal, Nat. Commun. **15**, 2174 (2024).

[13] V. Peri, M. Serra-Garcia, R. Ilan, and S. D. Huber, Axial-field-induced chiral channels in an acoustic Weyl system, Nat. Phys. **15**, 357 (2019).

[14] J. Hu, S. Zhuang, and Y. Yang, Higher-Order Topological Insulators via Momentum-Space Nonsymmorphic Symmetries, Phys. Rev. Lett. **132**, 213801 (2024).

[15] Y. Yang, B. Yang, G. Ma, J. Li, S. Zhang, and C. T. Chan, Non-Abelian physics in light and sound, Science **383**, eadf9621 (2024).

[16] Q. Guo, T. Jiang, R.-Y. Zhang, L. Zhang, Z.-Q. Zhang, B. Yang, S. Zhang, and C. T. Chan, Experimental observation of non-Abelian topological charges and edge states, Nature **594**, 195 (2021).

[17] T. Jiang, Q. Guo, R.-Y. Zhang, Z.-Q. Zhang, B. Yang, and C. T. Chan, Four-band non-Abelian topological insulator and its experimental realization, Nat. Commun. **12**, 6471 (2021).

[18] Z. Chen, R. Zhang, C. T. Chan, and G. Ma, Classical non-Abelian braiding of acoustic modes, Nat. Phys. **18**, 179 (2022).

[19] Y.-K. Sun, X.-L. Zhang, F. Yu, Z.-N. Tian, Q.-D. Chen, and H.-B. Sun, Non-Abelian Thouless pumping in photonic waveguides, Nat. Phys. **18**, 1080 (2022).

[20] X.-L. Zhang, F. Yu, Z.-G. Chen, Z.-N. Tian, Q.-D. Chen, H.-B. Sun, and G. Ma, Non-Abelian braiding on photonic chips, Nat. Photonics **16**, 390 (2022).

[21] B. Jiang, A. Bouhon, Z. Lin, X. Zhou, B. Hou, F. Li, R. Slager, and J. Jiang, Experimental observation of non-Abelian topological acoustic semimetals and their phase transitions, Nat. Phys. **17**, 1239 (2021).

[22] Q. Liang, Z. Dong, J. Pan, H. Wang, H. Li, Z. Yang, W. Yi, and B. Yan, Chiral dynamics of ultracold atoms under a tunable SU(2) synthetic gauge field, Nat. Phys. **20**, 1738 (2024).

[23] Q. Yan, Z. Wang, D. Wang, C. Lu, G. Ma, and Q. Gong, Non-Abelian gauge field in optics, Adv. Opt. Photonics **15**, 907 (2023).

[24] Y. Chen, R.-Y. Zhang, Z. Xiong, Z. H. Hang, J. Li, J. Q. Shen, and C. T. Chan, Non-Abelian gauge field optics, Nat. Commun. **10**, 3125 (2019).

[25] D. Cheng, K. Wang, C. Roques-Carmes, E. Lustig, O. Y. Long, H. Wang, and S. Fan, Non-Abelian lattice gauge fields in photonic synthetic frequency dimensions, Nature **637**, 52 (2025).

[26] J. Wu et al., Non-Abelian gauge fields in circuit systems, Nat. Electron. **5**, 635 (2022).

[27] L. Qian, W. Zhang, H. Sun, and X. Zhang, Non-Abelian Topological Bound States in the Continuum, Phys. Rev. Lett. **132**, 046601 (2024).

[28] X. Chen, J. Wu, X. Chen, Z. Pu, Y. Hu, J. Lu, M. Ke, W. Deng, and Z. Liu, Implementing Non-Abelian Hatano-Nelson Model in Electric Circuits, Phys. Rev. Lett. **136**, 106604 (2026).

[29] V. Neef, J. Pinske, F. Klauck, L. Teuber, M. Kremer, M. Ehrhardt, M. Heinrich, S. Scheel, and A. Szameit, Three-dimensional non-Abelian quantum holonomy, Nat. Phys. **19**, 30 (2023).

[30] Y. Chen et al., High-dimensional non-Abelian holonomy in integrated photonics,

Nat. Commun. **16**, 3650 (2025).

[31] Y. Yang, C. Peng, D. Zhu, H. Buljan, J. D. Joannopoulos, B. Zhen, and M. Soljačić, Synthesis and observation of non-Abelian gauge fields in real space, Science **365**, 1021 (2019).

[32] M. Iqbal et al., Non-Abelian topological order and anyons on a trapped-ion processor, Nature **626**, 505 (2024).

[33] S. Ma, H. Jia, Y. Bi, S. Ning, F. Guan, H. Liu, C. Wang, and S. Zhang, Gauge Field Induced Chiral Zero Mode in Five-Dimensional Yang Monopole Metamaterials, Phys. Rev. Lett. **130**, 243801 (2023).

[34] S. Sugawa, F. Salces-Carcoba, A. R. Perry, Y. Yue, and I. B. Spielman, Second Chern number of a quantum-simulated non-Abelian Yang monopole, Science **360**, 1429 (2018).

[35] Y. Yang, B. Zhen, J. D. Joannopoulos, and M. Soljačić, Non-Abelian generalizations of the Hofstadter model: spin–orbit-coupled butterfly pairs, Light Sci. Appl. **9**, 177 (2020).

[36] D. Cheng, K. Wang, and S. Fan, Artificial Non-Abelian Lattice Gauge Fields for Photons in the Synthetic Frequency Dimension, Phys. Rev. Lett. **130**, 083601 (2023).

[37] V. Liu, Y. Yang, J. D. Joannopoulos, and M. Soljačić, Three-dimensional non-Abelian generalizations of the Hofstadter model: Spin-orbit-coupled butterfly trios, Phys. Rev. B **104**, 115127 (2021).

[38] F. Chen, W.-W. Luo, W. Zhu, and D. N. Sheng, Robust non-Abelian even-denominator fractional Chern insulator in twisted bilayer MoTe2, Nat. Commun. **16**, 2115 (2025).

[39] C. N. Yang and R. L. Mills, Conservation of Isotopic Spin and Isotopic Gauge Invariance, Phys. Rev. **96**, 191 (1954).

[40] L. B. Zhang, F. Cheng, F. Zhai, and K. Chang, Electrical switching of the edge channel transport in HgTe quantum wells with an inverted band structure, Phys.

Rev. B **83**, 081402 (2011).

[41] P. Sternativo and F. Dolcini, Tunnel junction of helical edge states: Determining and controlling spin-preserving and spin-flipping processes through transconductance, Phys. Rev. B **89**, 035415 (2014).

[42] See Supplemental Material for (i) Hamiltonians for Hofstadter model, (ii) The agreement between acoustic structures and tight-binding model, (iii) Hamiltonians for Hofstadter acoustic crystals, (iv) Structural parameters of the acoustic crystals, (v) Berry curvature and topological invariants, (vi) Acoustic unit cells for Hofstadter butterfly, (vii) Simulations, (viii) Robustness of the non-Abelian boundary states, (ix) Spin-rotation boundary states under different non-Abelian gauge fields, (x) Spin-rotation boundary states with different boundary types, (xi) Measured Abelian and non-Abelian boundary states along the x direction, (xii) Boundaries of the narrow bridge, (xiii) Bridge-width modulated transmission in H-shaped waveguides.

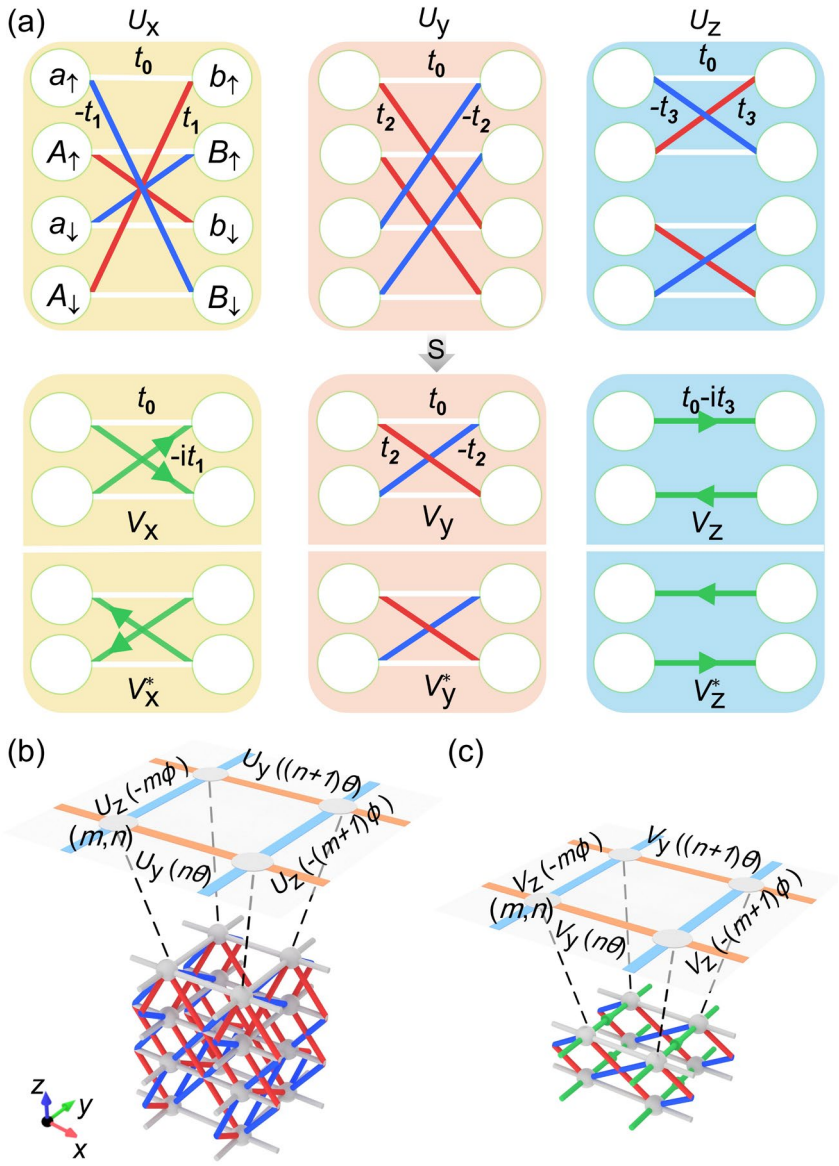

Fig. 1 Implementation of artificial SU(2) gauge fields. (a) Tight-binding model for creating arbitrary artificial SU(2) gauge fields. (b) Non-Abelian Hofstadter model realized through purely real couplings. (c) Non-Abelian Hofstadter model with complex matrix couplings in the $|+\mathrm{i}\rangle$ subspace.

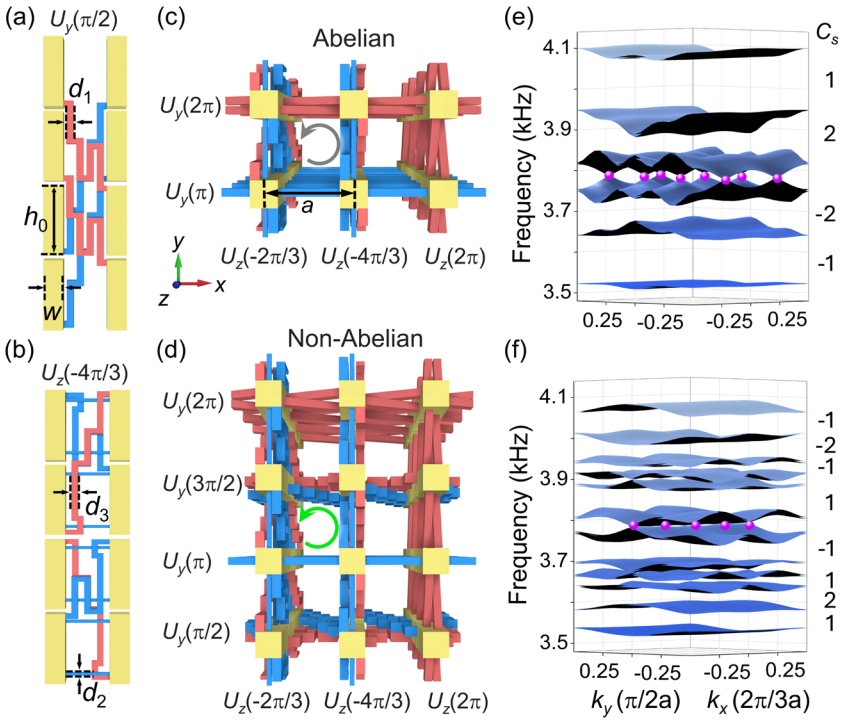

Fig. 2 Acoustic topological insulators induced by artificial Abelian and non-Abelian gauge fields. Acoustic implementation of link variables (a) $U_y(\pi/2)$ and (b) $U_z(-4\pi/3)$. Acoustic crystals for (c) Abelian $(\theta,\phi)=(\pi,2\pi/3)$ and (d) non-Abelian $(\theta,\phi)=(\pi/2,2\pi/3)$ Hofstadter models. The gray and green loops denote Abelian and non-Abelian Wilson loop, respectively. Bulk band dispersions for (e) Abelian and (f) non-Abelian topological insulators.

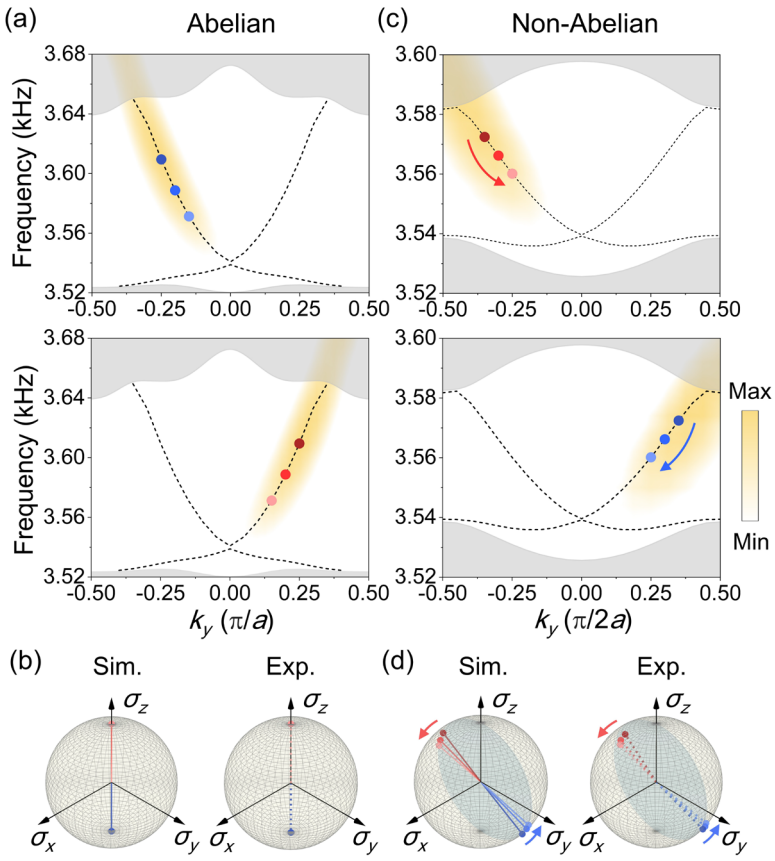

405

406 **Fig. 3 Acoustic Abelian and non-Abelian boundary states.** (a) Measured dispersions
407 of a pair of *y*-direction helical boundary states, and (b) their spin projections for Abelian
408 case. (c) Measured dispersions of a pair of helical boundary states, and (d) their spin
409 projections with spin-rotation characteristics for non-Abelian case.

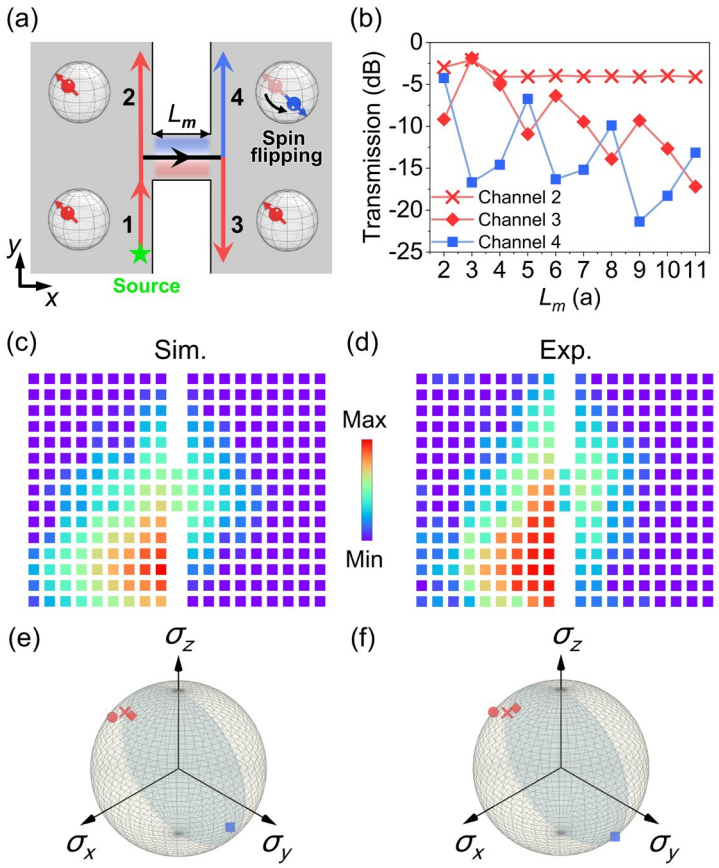

410

411 **Fig. 4 Spin flipping in an H-shaped non-Abelian acoustic crystal.** (a) Schematic of

412 the H-shaped structure. L_m is the bridge length. (b) Simulated transmission from

413 channel 1 to channel 2, 3 and 4 with different L_m. (c) Simulated and (d) measured

414 acoustic field distributions for $L_m = 2a$. (e) Simulated and (f) measured spin

415 polarization of the transmission fields extracted from the four channels.

416 **End Matter**

417 *Wilson loop* ------ The magnetic-field effect of the non-Abelian Hofstadter model can

418 be obtained by tracking the accumulated phase along a closed loop C of a square

419 plaquette. Such phase, known as non-Abelian holonomy, is obtained by evaluating the

420 Wilson loop $\boldsymbol{W}_{m,n} = \exp\left(i\oint_C \boldsymbol{A}\cdot d\boldsymbol{r}\right)$ counterclockwise around the plaquette, starting

421 from its lower-left corner site $\boldsymbol{r} = (m,n)$. From the commutation relations of the Wilson

422 loops, one can identify the nature of the artificial gauge fields [3,35]. In general, the

423 Wilson loop satisfies $\left[\boldsymbol{W}_{m,n}, \boldsymbol{W}_{m',n'}\right] \neq 0$ for $m \neq m'$ and $n \neq n'$, which indicates a non-

Abelian magnetic flux in the plaquette. However, when the values of (θ,ϕ) cause Wilson loop to satisfy $\left[\boldsymbol{W}_{m,n},\boldsymbol{W}_{m',n'}\right]=0$, the gauge field reduces to an Abelian case. Its Wilson loop is $\boldsymbol{W}_{m,n}=\begin{pmatrix} e^{i\alpha} & 0 \\ 0 & e^{-i\alpha} \end{pmatrix}$, indicating that different spins experience opposite magnetic fluxes α in the plaquette. From the commutation property of the Wilson loop, we can verify the nature of the gauge field constructed by the non-Abelian Hofstadter model: it remains predominantly non-Abelian for most parameter values (θ,ϕ), but reduces to an Abelian one at certain special parameter values, i.e. $\theta\in\{0,\ \pi\}$, $\phi\in\{0,\ \pi\}$, or $\{\theta,\ \phi\}\in\{\pi/2,\ 3\pi/2\}$ [3,35].

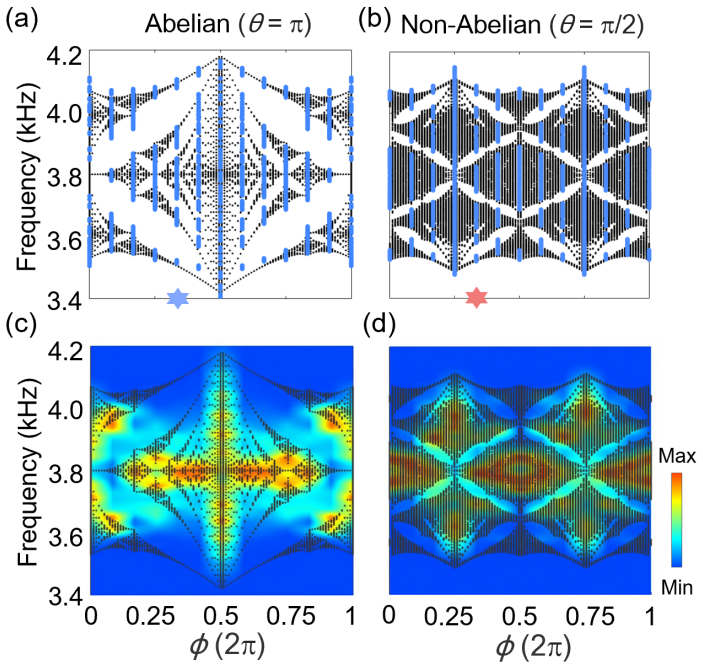

Fig. 5 Acoustic Abelian and non-Abelian Hofstadter butterflies. (a), (b) Acoustic Hofstadter butterflies as a function of ϕ for Abelian and non-Abelian cases, respectively. (c), (d) The simulated acoustic transmission spectra for Abelian and non-Abelian cases, respectively.

Acoustic Hofstadter butterfly spectrum------By fixing $\theta=\pi$ and $\theta=\pi/2$, we design a series of acoustic unit cells (see details in Supplemental Material Sec. VI [42]),

where flux ϕ is tuned from 0 to 2π in discrete steps of $\pi/6$ by precisely engineering the coupling strength, corresponding to the artificial Abelian and non-Abelian cases, respectively. For the Abelian case, the eigenfrequency spectrum as a function of the flux ϕ is plotted in Fig. 5(a). The black and blue dots represent the results from tight-binding model and simulations, respectively. The detailed parameters for tight-binding model are provided in Supplemental Material Sec. VII [42]. The fractal shape corresponding to the Abelian Hofstadter butterfly of QSHE, which describes spin-1/2 electrons in a uniform strong magnetic field with different strengths. Owing to the time-reversal symmetry and spin conservation, the two spin spaces decouple into two time-reversed copies of the Hofstadter butterfly. For the non-Abelian case, the butterfly spectrum exhibits more complex fractal features with a set of narrow nested gaps, as shown in Fig. 5(b). Compared with the Abelian case, the non-Abelian magnetic field exerts a significant influence on the fractal characteristics and multi-energy gap structure of the butterfly spectrum. The values of θ and ϕ corresponding to the blue and red stars are adopted in the experiments.

Furthermore, the transmission of the butterfly spectrum also reveals distinct differences between the two fractal structures. Finite acoustic structures with the size of $12a \times 12a$ are used to numerically simulate the transmission spectrum. Using full-wave simulations, we excite each finite acoustic structure at the bottom boundary and extract the transmitted acoustic pressure at the top boundary. We record the simulated transmission spectrum as a function of flux ϕ under different gauge fields. In the Abelian gauge fields, the simulated transmission spectra (colormaps) of the Hofstadter acoustic crystals are shown in Fig. 5(c). As expected, the transmission spectra clearly reveal the characteristic outline of the Abelian Hofstadter butterfly (black dots). In the non-Abelian gauge fields, the simulated transmission spectra reproduce a more complex nested fractal structure of the non-Abelian Hofstadter butterfly, as shown in Fig. 5(d). The simulated transmission spectra of the Hofstadter acoustic crystals are in

good agreement with the theoretical results, demonstrating that this design method is effective for exploring artificial non-Abelian gauge fields in spinless systems.

Experiments------Abelian and non-Abelian acoustic samples are fabricated via 3D printing using UV resin, as shown in Figs. 6(a) and 6(b), respectively. For the Abelian topological insulator, the truncated *y*- and *x*-boundaries along the *x* and *y* directions are located at link variables $U_z(2\pi)$ and $U_y(\pi)$, respectively; for non-Abelian topological insulator, they are located at $U_z(2\pi)$ and $U_y(\pi/2)$, respectively, as represented by the red boxes. Acoustic signals are generated by a B&K network analyzer (B&K Type 3160), then split into four channels, with their amplitudes independently controlled by power amplifiers and their phases independently adjusted using phase shifters. Four balanced armature speakers (Knowles WBFK30095) are placed at the hard boundary, one in each layer, as sound sources. A sub-wavelength microphone probe (B&K Type 4961) is used to probe the pressure response, and the pressure signals are recorded by an oscilloscope (RIGOL HDO4204). To measure the projected band dispersions along the k_x and k_y directions, the sound sources are placed at the *x*- and *y*-boundaries of the samples depicted in Figs. 6(a) and 6(b). To probe the boundary states with $k_x > 0$ ($k_x < 0$), the sound sources are placed on the left (right) sides of the *x* boundary in each layer. Similarly, to measure the boundary states with $k_y > 0$ ($k_y < 0$), the sound sources are placed on the lower (upper) of the *y*-boundary in each layer. The sound pressure field $\psi_L(m,\omega)$ at each frequency along *x*- or *y*-boundary can be obtained by measuring the sound pressure in each cavity layer by layer along the boundary, where *m* denotes the site of the *L*-th layer along the *x* or *y* direction. The sound pressure response $\varphi_{\pm}(m,\omega)$ in the subspace $|\pm\mathrm{i}\rangle$ can be obtained through a unitary transformation $(\varphi_+(m,\omega),\varphi_-(m,\omega))^{\mathrm{T}} = S_1\boldsymbol{\psi}(m,\omega)$, where $S_1 = \frac{1}{\sqrt{2}}\begin{pmatrix}1 & \mathrm{i}\\ 1 & -\mathrm{i}\end{pmatrix}\otimes \mathrm{I}_2$ and

$\boldsymbol{\psi}(m,\omega)=(\psi_1(m,\omega),\psi_2(m,\omega),\psi_3(m,\omega),\psi_4(m,\omega))^{\mathrm{T}}$. Here, we focus on a single subspace $|+\mathrm{i}\rangle$. The projected band dispersions are obtained by applying fast Fourier transformation to the sound pressure field distributions $\varphi_+(m,\omega)$, yielding the momentum-space fields $\varphi_+(k_\mu,\omega),\mu=x,y$. For a given wave vector k_μ , the spin polarizations of the helical boundary states along the *x* or *y* directions are derived by projecting them onto the Bloch sphere $\langle\sigma_\alpha\rangle=\langle\varphi_+(k_\mu,\omega)|\sigma_\alpha|\varphi_+(k_\mu,\omega)\rangle$. The acoustic pressure field distributions of the H-shaped structure in Fig. 4(d) are measured by placing sound sources at the position denoted as a green star in Fig. 4(a). The acoustic pressure in each cavity on the top layer is then measured sequentially using the microphone probe.

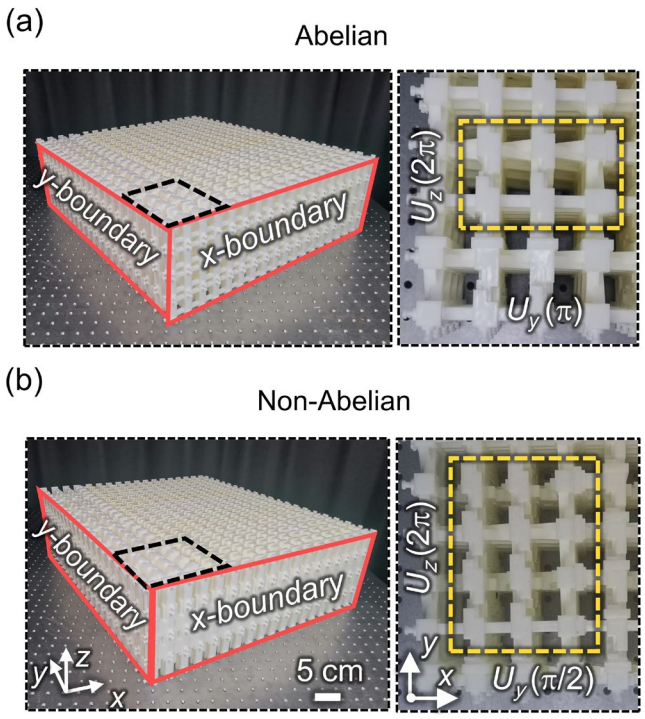

Fig. 6 Abelian and non-Abelian acoustic samples. Photographs of (a) the Abelian and (b) non-Abelian topological insulator samples. The yellow box highlights a unit cell.